Philosophical Magazine
Vol. 00, No. 00, 00 Month 200x, 1–15

RESEARCH ARTICLE

Analytical computation of the lattice rotations induced by 3D dislocation loops

Felix Hofmann[a], Sinead Keegan[b] and Alexander M Korsunsky [a]

[a]*Department of Engineering Science, University of Oxford, Parks Road, OX1 3PJ, UK*;
[b]*School of Theoretical Physics, Dublin Institute for Advanced Studies, 10 Burlington Road, Dublin 4, Ireland*

(*Received 00 Month 200x; final version received 00 Month 200x*)

This paper presents the derivation of expressions for the lattice rotations induced by a triangular dislocation loop in an isotropic, elastic medium, based on the classical displacement field solution for a triangular dislocation loop. Using the simple example of a triangular dislocation loop with one segment of edge character, one segment of screw character and a mixed character segment, a comparison of the $3D$ lattice rotation fields with those predicted for straight, infinitely long $2D$ dislocations is made. Agreement is excellent.

As an illustration of the utility of the rotation solution, the lattice rotations induced by a Frank-Read Source are studied at different stages during its evolution. The dislocation segment positions were computed using the discrete dislocation dynamics code ParaDiS. Post-processing of the lattice rotation maps in terms of lattice orientation spread reveals preferential lattice misorientation or streaking which is consistent with the single active slip system in the simulation. Streaking is a feature frequently observed in micro-diffraction measurements.

The availability of the lattice rotation solution makes it possible to evaluate the lattice rotations arising from any $3D$ distribution of dislocation segments. This allows the computation of predicted diffraction patterns from computed dislocation substructures for direct comparison with experimental measurements. It also makes the inclusion of lattice rotations into $3D$ dislocation dynamics codes possible. This effect has thus far been treated as small, but was shown to be important in $2D$ dislocation dynamics simulations.

Keywords: here provide 3 to 10 keywords for the article

1. Introduction

The formation of dislocation substructures in FCC metals is well-documented [1–3]. As deformation is applied to a polycrystalline sample, the evolution of dislocation density is non-uniform within the constituent grains. Dislocations are found to arrange themselves into cell/wall type structures where high dislocation density walls separate low dislocation density subgrains [4]. The spatial distribution of dislocations can be investigated post mortem at high resolution by transmission electron microscopy (TEM) [5]. However the dislocation dynamics observed by TEM are not representative of the bulk due to the artefacts arising from the very thin sections which have to be considered.

X-ray diffraction provides an alternative, powerful tool for the study of dislocation substructure formation within individual crystallites embedded in the bulk of the material. Modern third generation synchrotron x-ray sources allow high spatial resolution mapping of the relative lattice rotations which arise between adjacent subgrains due to the geometrically necessary dislocation (GND) component of the dislocation population in the cell walls. Reciprocal space mapping (RSM)

ISSN: 1478-6435 print/ISSN 1478-6443 online

DOI: 10.1080/1478643YYxxxxxxxx
http://www.informaworld.com

is a technique which is particularly well-suited to this purpose [6]. Diffraction of a monochromatic x-ray beam is used to map a particular Bragg reflection arising from a single crystal within the bulk in all three reciprocal space directions. By tilting the sample, the variation of scattered intensity can be probed as a function of the scattering vector orientation, and hence the local spread of lattice orientation deduced. Varying the angular positioning of the detector and sample in a "θ - 2θ" type scan changes the length of the scattering vector and allows the determination of lattice spacing for that particular radial reciprocal space direction. Hence the elastic strain in this direction can be determined [7].

RSM has been applied to the study of dislocation substructure evolution in a single grain of copper within a polycrystalline specimen. Maps of intensity projected onto the tangential reciprocal space directions show that the initially sharp single reflection from the un-deformed grain breaks up into a number of sharp peaks superimposed on a background of enhanced intensity [6]. The sharp peaks arise from individual subgrains, whilst the background of enhanced intensity is due to the dislocation-rich cell walls. As tensile deformation is applied, the sharp peaks display dynamic behaviour which corresponds to subgrain rotation. By line profile analysis of intensity variation in the radial reciprocal space direction, elastic strain within the dislocation depleted subgrains can be determined. On average dislocation cells appear to experience compressive elastic strains whilst dislocation walls exhibit tensile strains [8, 9]. Over longer timescales, a "cleanup" of the dislocation structure has been observed, with subgrain peaks narrowing in all three reciprocal space directions, indicating a diffusion of dislocation from the subgrains to the dislocation rich cell walls. On unloading, the number of subgrain peaks remains the same, which suggests that the introduced dislocation substructure is stable [10].

Similar variations of diffraction peak shape, due to a spread of lattice orientations within the scattering volume, have been observed by micro-beam Laue diffraction. Here a polychromatic X-ray beam with a smooth photon energy spectrum, e.g. ranging from 5 - 10 keV to 22 -35 keV, is used to illuminate a gauge volume within a single crystal of a polycrystalline sample placed in reflection geometry [11, 12]. The diffraction pattern consisting of a large number of Laue diffraction spots is collected on an area detector placed above the sample with a the detector centre position corresponding to a scattering angle of $2\theta = 90°$. From the ensemble of the recorded Laue spot positions the lattice orientation and deviatoric elastic strain tensor averaged over the scattering volume can be determined. During deformation the shape of each Laue spot captures the spread of lattice orientation in the scattering volume. The misorientation measured by micro-beam Laue diffraction is the same as that measured by RSM, however at much lower angular resolution. Unlike RSM, micro-beam Laue diffraction does not allow access to the radial reciprocal space component of the reflection, unless the incident beam energy is analysed [13]. During deformation of a polycrystalline sample different responses can be observed in the constituent grains as a function of their lattice orientation. Laue spots from grains that are unfavorably oriented for slip will show almost no modification, whilst those arising from grains oriented more favorably for slip may show some fragmentation or streaking [14]. Streaked patterns can be interpreted in terms of the lattice rotation arising from a population of edge dislocations on a particular slip plane. Hence the active slip system can be determined [15]. Discontinuities within a streak arise due to non-uniformity of the rotation gradient within the scattering volume, which in turn can be simulated by assuming some non-uniformity in the distribution of edge dislocations and introducing geometrically necessary boundaries (GNBs) [16, 17]. A similar forward modelling approach has been shown capable of capturing some of the features observed in reciprocal

space maps of samples with a dislocation cell/wall type substructure [18].

In this type of modelling approach, a dislocation substructure is postulated, a forward model of the diffraction pattern established and then compared to the experimental diffraction pattern. The postulated dislocation substructure is then modified so as to achieve the best match with the measured diffraction pattern. When some non-uniformity is present within the experimental diffraction pattern, the solution of the underlying dislocation structure is non-unique, i.e. a number of different possible dislocation arrangements could give rise to the same reciprocal space map. To gain a deeper physical insight into the underlying dislocation interactions which give rise to the formation of dislocation cell/wall patterns, any forward model that is established has to be based on a physically meaningful mechanical model.

Recently it has been successfully shown that the peak shape evolution within individual grains of a polycrystalline Ni sample can be captured successfully by diffraction post-processing of a crystal plasticity model of the sample geometry [19]. A limitation of this approach is that it is not capable of capturing the effects of dislocation substructure formation, but rather only the gradual mis-orientations that arise from smoothly varying dislocation distributions. In order to capture the effects of non-uniform dislocation arrangements, the prediction of reciprocal space maps should be carried out based on the dislocation arrangements computed from dislocation dynamics simulations.

There are a number of different approaches to dislocation dynamics modelling. Van der Giessen and Needleman [20] have proposed a 2D approach, modelling deformation by the motion of edge dislocations along discrete predefined slip systems. Dislocations are introduced from a number of randomly distributed sources and their motion and interaction is governed by a set of constitutive rules. Suitable boundary conditions are imposed upon the simulation by a finite element model which provides a continuous stress field superimposed on the dislocation stress field to produce the total stress field at each time step. This model has been applied to a wide range of problems from thin films [21–23] to nano-indentation [24–27] and fatigue crack growth [28, 29]. It has also been shown capable of reproducing grain size dependent Hall-Petch type hardening behaviour[30, 31] and the orientation dependance of yield [32]. The great advantage of this approach is that it is comparatively straightforward to implement and computationally inexpensive. However it remains very much limited in that it only considers the $2D$ problem, although some efforts have gone towards the inclusion of $3D$ effects [33].

Arsenlis et al. [34–36] proposed an alternative, more general framework for the modelling of dislocation motion in three dimensions. Dislocations are treated as line defects moving within an elastic continuum. For the purposes of computation, each dislocation line is divided into straight segments, each carrying a Burgers vector and connecting 2 nodes. The computation of forces acting on each dislocation segment is carried out at the nodal points. From these forces the motion of the dislocation line is computed using a mobility function approach [34, 37]. Dislocation core interactions are implemented in the form of a set of constitutive rules dealing with splitting, recombination and annihilation. This discrete dislocation dynamics simulation framework has been implementation numerically in the ParaDiS (Parallel Dislocation Simulator) code. Due to the complexity of the model, computational efficiency is a very important consideration and the code has been optimized for the operation on large supercomputing facilities, although simple examples as illustrated below can be run on a normal desktop computer [34]. This model has been shown capable of generating a very realistic stress strain response for single crystals [35] and has provided important physical insight into the role

played by multijunctions in controlling strain hardening [38].

To compute the diffraction patterns from a given $3D$ dislocation structure, a solution for the rotation field induced by a dislocation segment is essential. In this paper we present the derivation of the rotation field arising from a dislocation triangle ABC based on the displacement field solution for isotropic elasticity given by Barnett and Balluffi [39, 40], which is an adaptation of the solution given by Hirth and Lothe [41]. For the purposes of validation and illustration the rotation solution is applied to the simple example of a triangular dislocation loop with one edge dislocation segment, one screw dislocation segment and one mixed dislocation segment. Comparison of the edge and screw dislocation fields with the rotation field induced by an infinite edge and screw dislocation respectively shows excellent agreement. Next, the rotation fields arising from a Frank-Read Source at different stages during its evolution are computed based on dislocation positions calculated using the ParaDiS dislocation dynamics simulation code. The rotations maps and the spread of lattice rotations can be linked to the streaking frequently observed in diffraction measurements and interpreted in terms of the active slip system(s).

2. Derivation of the analytical expression of rotation due to a triangular dislocation loop

Following the notation of Barnett and Balluffi [39, 40], let ABC be a triangular dislocation loop and P be a field point. $\mathbf{R}_A$, $\mathbf{R}_B$, $\mathbf{R}_C$ denote the vectors from P to the vertices A, B, C respectively. Ω denotes the solid angle associated with the triangle ABC, as seen by an observer at P. Then the loop displacement field is given by

$$\mathbf{u}(P) = -\frac{\mathbf{b}\Omega}{4\pi} + \mathbf{F}_{AB} + \mathbf{F}_{BC} + \mathbf{F}_{CA}, \tag{1}$$

where

$$\mathbf{F}_{AB} = -\frac{(1-2\nu)}{8\pi(1-\nu)}\left(\mathbf{b}\wedge\mathbf{t}_{AB}\right)R_B + \ln\left(\frac{R_B+\mathbf{R}_B\cdot\mathbf{t}_{AB}}{R_A+\mathbf{R}_A\cdot\mathbf{t}_{AB}}\right) + \frac{1}{8\pi(1-\nu)}\left(\mathbf{b}\cdot\mathbf{n}_{AB}\right)\left(\boldsymbol{\lambda}_B-\boldsymbol{\lambda}_A\right)\wedge\mathbf{n}_{AB}, \tag{2}$$

and

$$\mathbf{n}_{AB} = \frac{\boldsymbol{\lambda}_A\wedge\boldsymbol{\lambda}_B}{|\boldsymbol{\lambda}_A\wedge\boldsymbol{\lambda}_B|}. \tag{3}$$

Cyclic interchange of A, B, C in equations (2) and (3) results in expressions for $\mathbf{F}_{BC}$ and $\mathbf{F}_{CA}$. R_A, R_B, R_C denote the magnitudes of $\mathbf{R}_A$, $\mathbf{R}_B$, $\mathbf{R}_C$ respectively, and $\boldsymbol{\lambda}_A$, $\boldsymbol{\lambda}_B$, $\boldsymbol{\lambda}_C$ denote unit vectors in the $\mathbf{R}_A$, $\mathbf{R}_B$, $\mathbf{R}_C$ directions respectively. $\mathbf{t}_{AB}$, $\mathbf{t}_{BC}$, $\mathbf{t}_{CA}$ denote unit tangents along $\mathbf{AB}$, $\mathbf{BC}$, $\mathbf{CA}$ respectively. ν is Poisson's ratio, and $\mathbf{b}$ the loop Burgers vector.

The solid angle Ω is given by the equation

$$\Omega = -\mathrm{sgn}\left(\boldsymbol{\lambda}_A\cdot\mathbf{N}\right)E, \tag{4}$$

where $\mathbf{N}$ is a unit normal to the ABC plane, chosen such that an observer looking in the direction $-\mathbf{N}$ sees ABC in an anti-clockwise direction. In our calculations

we define

$$\mathbf{N} = \frac{\mathbf{t}_{AB} \wedge \mathbf{t}_{BC}}{|\mathbf{t}_{AB} \wedge \mathbf{t}_{BC}|}. \tag{5}$$

The quantity E is computed using the equation

$$E = 4 \arctan \sqrt{\tan\left(\frac{s}{2}\right) \tan\left(\frac{s-a}{2}\right) \tan\left(\frac{s-b}{2}\right) \tan\left(\frac{s-c}{2}\right)}, \tag{6}$$

where a is defined by

$$a = \arccos\left(\boldsymbol{\lambda}_B \cdot \boldsymbol{\lambda}_C\right), \tag{7}$$

and b and c are obtained by cyclic interchange in equation (7) in the obvious way. The quantity s is defined as

$$s = \frac{1}{2}\left(a + b + c\right). \tag{8}$$

The aim of the present study is to calculate the derivatives of the loop displacement field $\mathbf{u}(P)$ with respect to x, y, and z respectively, so that the small rotation angles can be computed. In the following equations ξ can be replaced by either x, y or z.

The derivative of $\mathbf{F}_{AB}$ is given by

$$\begin{aligned}\frac{\partial \mathbf{F}_{AB}}{\partial \xi} = &-\frac{(1-2\nu)}{8\pi(1-\nu)}\left(\frac{\frac{\partial \mathbf{R}_B}{\partial \xi} + \frac{\partial \mathbf{R}_B}{\partial \xi} \cdot \mathbf{t}_{AB}}{R_B + \mathbf{R}_B \cdot \mathbf{t}_{AB}} - \frac{\frac{\partial \mathbf{R}_A}{\partial \xi} + \frac{\partial \mathbf{R}_A}{\partial \xi} \cdot \mathbf{t}_{AB}}{R_A + \mathbf{R}_A \cdot \mathbf{t}_{AB}}\right) \\ &+ \frac{(\mathbf{b} \cdot \mathbf{n}_{AB})}{8\pi(1-\nu)}\left((\boldsymbol{\lambda}_B - \boldsymbol{\lambda}_A) \wedge \frac{\partial \mathbf{n}_{AB}}{\partial \xi} + \left(\frac{\partial \boldsymbol{\lambda}_B}{\partial \xi} - \frac{\partial \boldsymbol{\lambda}_A}{\partial \xi}\right) \wedge \mathbf{n}_{AB}\right) \\ &+ \frac{1}{8\pi(1-\nu)}\left(\mathbf{b} \cdot \frac{\partial \mathbf{n}_{AB}}{\partial \xi}\right)\left((\boldsymbol{\lambda}_B - \boldsymbol{\lambda}_A) \wedge \mathbf{n}_{AB}\right),\end{aligned} \tag{9}$$

where

$$\frac{\partial \mathbf{R}_A}{\partial x} = (-1, 0, 0), \tag{10}$$

$$\frac{\partial \mathbf{R}_A}{\partial y} = (0, -1, 0), \tag{11}$$

$$\frac{\partial \mathbf{R}_A}{\partial z} = (0, 0, -1), \tag{12}$$

$$\frac{\partial R_A}{\partial \xi} = \frac{\xi - A_\xi}{R_A}, \tag{13}$$

$$\frac{\partial \boldsymbol{\lambda}_A}{\partial \xi} = \frac{R_A \frac{\partial \mathbf{R}_A}{\partial \xi} - \frac{\partial R_A}{\partial \xi}\mathbf{R}_A}{(R_A)^2}. \tag{14}$$

and A can be replaced by B or C as appropriate. In equation (13), A_ξ denotes the ξ^{th} component of A. The following derivatives also appear in equation (9).

$$\frac{\partial \left|\boldsymbol{\lambda}_A \wedge \boldsymbol{\lambda}_B\right|}{\partial \xi} = \mathbf{n}_{AB} \cdot \frac{\partial \left(\boldsymbol{\lambda}_A \wedge \boldsymbol{\lambda}_B\right)}{\partial \xi}, \tag{15}$$

$$\frac{\partial \left(\boldsymbol{\lambda}_A \wedge \boldsymbol{\lambda}_B\right)}{\partial \xi} = \boldsymbol{\lambda}_A \wedge \frac{\partial \boldsymbol{\lambda}_B}{\partial \xi} + \frac{\partial \boldsymbol{\lambda}_A}{\partial \xi} \wedge \boldsymbol{\lambda}_B, \tag{16}$$

$$\frac{\partial \mathbf{n}_{AB}}{\partial \xi} = \frac{1}{\left|\boldsymbol{\lambda}_A \wedge \boldsymbol{\lambda}_B\right|} \frac{\partial \left(\boldsymbol{\lambda}_A \wedge \boldsymbol{\lambda}_B\right)}{\partial \xi} - \frac{\left(\boldsymbol{\lambda}_A \wedge \boldsymbol{\lambda}_B\right)}{\left|\boldsymbol{\lambda}_A \wedge \boldsymbol{\lambda}_B\right|^2} \frac{\partial \left|\boldsymbol{\lambda}_A \wedge \boldsymbol{\lambda}_B\right|}{\partial \xi}. \tag{17}$$

The derivatives of $\mathbf{F}_{BC}$ and $\mathbf{F}_{CA}$ are obtained by cyclic interchange of A, B, C in the above equations.

In order to compute the derivative of $\mathbf{u}(P)$ it is also necessary to differentiate the quantity E. This is done as follows.

$$\begin{aligned}
\frac{\partial E}{\partial \xi} = \Bigg[& \sec^2\left(\frac{s}{2}\right) \tan\left(\frac{s-a}{2}\right) \tan\left(\frac{s-b}{2}\right) \tan\left(\frac{s-c}{2}\right) \frac{\partial s}{\partial \xi} \\
& + \sec^2\left(\frac{s-a}{2}\right) \tan\left(\frac{s}{2}\right) \tan\left(\frac{s-b}{2}\right) \tan\left(\frac{s-c}{2}\right) \frac{\partial (s-a)}{\partial \xi} \\
& + \sec^2\left(\frac{s-b}{2}\right) \tan\left(\frac{s}{2}\right) \tan\left(\frac{s-a}{2}\right) \tan\left(\frac{s-c}{2}\right) \frac{\partial (s-b)}{\partial \xi} \\
& + \sec^2\left(\frac{s-c}{2}\right) \tan\left(\frac{s}{2}\right) \tan\left(\frac{s-a}{2}\right) \tan\left(\frac{s-b}{2}\right) \frac{\partial (s-c)}{\partial \xi} \Bigg] \\
& \div \sec^2\left(\frac{E}{4}\right) \tan\left(\frac{E}{4}\right),
\end{aligned} \tag{18}$$

where

$$\frac{\partial a}{\partial \xi} = \frac{-1}{\left|\boldsymbol{\lambda}_B \wedge \boldsymbol{\lambda}_C\right|} \left(\frac{\partial}{\partial \xi} \left(\boldsymbol{\lambda}_B \cdot \boldsymbol{\lambda}_C\right)\right), \tag{19}$$

$$\frac{\partial b}{\partial \xi} = \frac{-1}{\left|\boldsymbol{\lambda}_C \wedge \boldsymbol{\lambda}_A\right|} \left(\frac{\partial}{\partial \xi} \left(\boldsymbol{\lambda}_C \cdot \boldsymbol{\lambda}_A\right)\right), \tag{20}$$

$$\frac{\partial c}{\partial \xi} = \frac{-1}{\left|\boldsymbol{\lambda}_A \wedge \boldsymbol{\lambda}_B\right|} \left(\frac{\partial}{\partial \xi} \left(\boldsymbol{\lambda}_A \cdot \boldsymbol{\lambda}_B\right)\right), \tag{21}$$

$$\frac{\partial s}{\partial \xi} = \frac{1}{2} \left(\frac{\partial a}{\partial \xi} + \frac{\partial b}{\partial \xi} + \frac{\partial c}{\partial \xi}\right), \tag{22}$$

$$\tag{23}$$

and

$$\frac{\partial}{\partial \xi}\left(\boldsymbol{\lambda}_A \cdot \boldsymbol{\lambda}_B\right) = \boldsymbol{\lambda}_A \cdot \frac{\partial \boldsymbol{\lambda}_B}{\partial \xi} + \boldsymbol{\lambda}_B \cdot \frac{\partial \boldsymbol{\lambda}_A}{\partial \xi}. \tag{24}$$

The derivative of Ω is given by

$$\frac{\partial \Omega}{\partial \xi} = -\mathrm{sgn}\left(\boldsymbol{\lambda}_A \cdot \mathbf{N}\right) \frac{\partial E}{\partial \xi} - 2\delta\left(\boldsymbol{\lambda}_A \cdot \mathbf{N}\right)\left(\frac{\partial \boldsymbol{\lambda}_A}{\partial \xi} \cdot \mathbf{N}\right) E. \tag{25}$$

where δ denotes the Dirac delta function. Finally, the derivative of $\mathbf{u}(P)$ is given by

$$\frac{\partial}{\partial \xi}\mathbf{u}(P) = -\frac{\mathbf{b}}{4\pi}\frac{\partial \Omega}{\partial \xi} + \frac{\partial \mathbf{F}_{AB}}{\partial \xi} + \frac{\partial \mathbf{F}_{BC}}{\partial \xi} + \frac{\partial \mathbf{F}_{CA}}{\partial \xi}. \tag{26}$$

where ξ denotes either x or y or z. The lattice rotations at field point P due to the presence of dislocation loop ABC are:

$$\omega_x = \frac{1}{2}\left(\frac{\partial u_z}{\partial y} - \frac{\partial u_y}{\partial z}\right), \tag{27}$$

$$\omega_y = \frac{1}{2}\left(\frac{\partial u_x}{\partial z} - \frac{\partial u_z}{\partial x}\right), \tag{28}$$

$$\omega_z = \frac{1}{2}\left(\frac{\partial u_y}{\partial x} - \frac{\partial u_x}{\partial y}\right). \tag{29}$$

where ω_x, ω_y and ω_z correspond to small rotations about the x, y and z axes respectively. u_x, u_y and u_z denote respectively the x, y and z components of $\mathbf{u}$. The elastic strains at field point P are given by:

$$\epsilon_{xx} = \frac{\partial u_x}{\partial x}, \quad \epsilon_{xx} = \frac{\partial u_x}{\partial x}, \quad \epsilon_{xx} = \frac{\partial u_x}{\partial x}, \tag{30}$$

$$\gamma_{xy} = \frac{\partial u_y}{\partial x} + \frac{\partial u_x}{\partial y}, \quad \gamma_{yz} = \frac{\partial u_z}{\partial y} + \frac{\partial u_y}{\partial z}, \quad \gamma_{zx} = \frac{\partial u_x}{\partial z} + \frac{\partial u_z}{\partial x}. \tag{31}$$

where ϵ_{xx}, ϵ_{yy} and ϵ_{zz} denote the direct elastic strains in the x, y and z direction respectively, and γ_{xy}, γ_{xy} and γ_{xy} give the shear strains.

In this paper we will focus on the lattice rotations induced by the presence of dislocations, as this quantity is most readily measured using high angular resolution synchrotron X-ray diffraction measurements.

3. Comparison with the analytical 2D lattice rotation solutions

In order to validate the correctness of the above solution for ω_x, ω_y and ω_z, comparisons with some simple, two-dimensional cases are made here. The elastic displacement field of an infinitely long edge dislocation in an isotropic elastic medium, running along the z-axis, with Burgers vector of magnitude b along the x-axis is given by:

$$\overline{u_x}_\perp = \frac{b}{2\pi}\left(\frac{xy}{2\left(x^2+y^2\right)^2(1-\nu)} + \arctan\frac{y}{x}\right), \tag{32}$$

$$\overline{u_y}_\perp = -\frac{b}{2\pi}\left(\frac{x^2-y^2}{4\left(x^2+y^2\right)^2(1-\nu)} + \frac{(1-2\nu)\ln\left(x^2+y^2\right)}{4(1-\nu)}\right), \tag{33}$$

$$\overline{u_z}_\perp = 0. \tag{34}$$

The differentiation of these quantities and substitution into equations (27) to (29) leads to the following expressions for the $2D$ rotation field:

$$\overline{\omega_x}_\perp = 0, \tag{35}$$

$$\overline{\omega_y}_\perp = 0, \tag{36}$$

$$\overline{\omega_z}_\perp = -\frac{b}{2\pi}\frac{x}{x^2+y^2}. \tag{37}$$

where $\overline{\omega_x}_\perp$, $\overline{\omega_y}_\perp$ and $\overline{\omega_z}_\perp$ are the lattice rotations about the x, y and z axis respectively. Similarly the deformation field for an infinitely long screw dislocation along the x-axis is given by the following expression:

$$\overline{u_x}_S = \frac{b}{2\pi}\arctan\left(\frac{z}{y}\right), \tag{38}$$

$$\overline{u_x}_S = 0, \tag{39}$$

$$\overline{u_x}_S = 0. \tag{40}$$

The differentiation and substitution into equations (27) to (29) leads to the following expressions for the $2D$ rotation field:

$$\overline{\omega_x}_S = 0, \tag{41}$$

$$\overline{\omega_y}_S = \frac{b}{4\pi}\frac{y}{y^2+z^2}, \tag{42}$$

$$\overline{\omega_z}_S = \frac{b}{4\pi}\frac{z}{y^2+z^2}. \tag{43}$$

where $\overline{\omega_x}_S$, $\overline{\omega_y}_S$ and $\overline{\omega_z}_S$ are the lattice rotations about the x, y and z axes respectively.

In order to test and validate the rotation expressions for a dislocation triangle ABC, it is instructive to consider a simple example in which pure edge, pure screw and mixed dislocation elements are present. The simplest structure for which this can be achieved is the dislocation triangle shown in figure 1**a)**. Here the dislocation loop consists of the three vertices A, B and C, placed at $[0,0,1000]$, $[0,0,0]$ and $[1000,0,0]$ respectively. Assigning a Burgers vector $\boldsymbol{b}$ of $[1,0,0]$, means that the segment AB is a pure edge dislocation, segment BC a pure screw dislocation and segment CA a mixed dislocation with both a screw and an edge components.

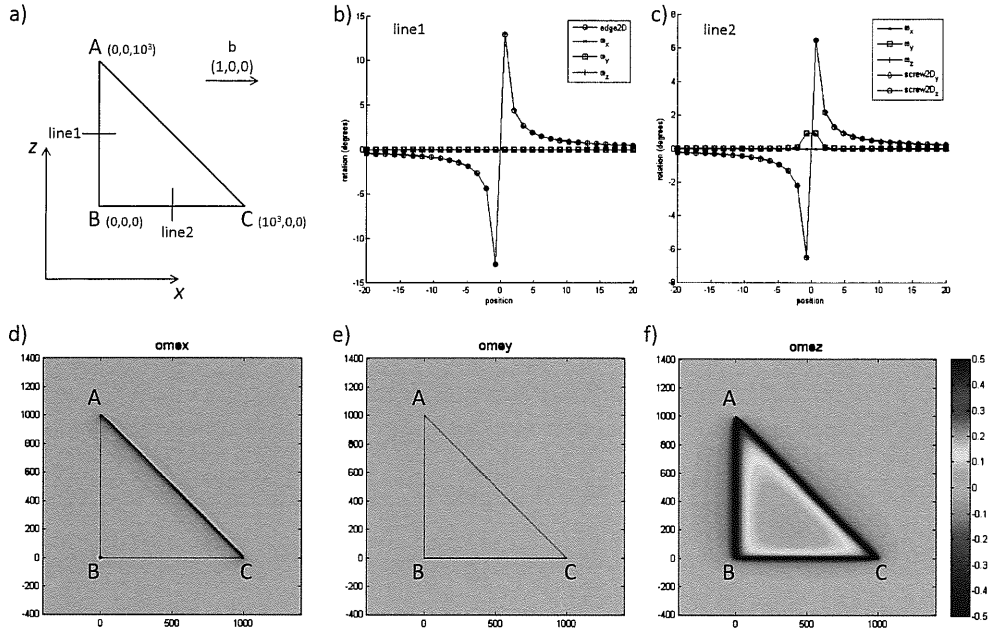

Figure 1. Consideration of a simple triangular dislocation loop ABC with Burgers vector $\boldsymbol{b}$. **a)** diagram of the dislocation loop, **b)** line plot of rotation along "line 1", showing ω_x, ω_y, ω_z and $\overline{\omega_z}_\perp$ **c)** line plot of rotation along "line 2", showing ω_x, ω_y, ω_z, $\overline{\omega_y}_S$ and $\overline{\omega_z}_S$ **d), e)** and **f)** show maps of ω_x, ω_y and ω_z rotation respectively for the dislocation loop in the xz plane, computed at $y = 0.1$.

Poisson's ration ν was taken as 0.3.

The length of segment AB is 1000 units, which is large compared to the Burgers vector magnitude of 1 unit. Hence the rotation field in the center of segment AB should be comparable to the rotation field of an infinite edge dislocation running along the z axis, with Burgers vector in the x direction (equations (35) to (37)). This comparison was carried out along a line from $[-20, 0.1, 500]$ to $[-20, 0.1, 500]$ - "line 1" in figure 1 **a)**. Figure 1 **b)** shows the variation of ω_x, ω_y and ω_z along this plotted with the corresponding $\overline{\omega_z}_\perp$ variation for an infinite edge dislocation. It can clearly be seen that ω_z and $\overline{\omega_z}_\perp$ show very good agreement as anticipated. ω_x and ω_y are both zero which is consistent with the values of $\overline{\omega_x}_\perp$ and $\overline{\omega_y}_\perp$ respectively as expect for an infinite edge dislocation.

Similarly, the length of segment BC of 1000 units is large compared to the Burgers vector. Hence the rotation field in the middle of segment BC should be well matched to the rotation field of an infinite screw dislocation along the x axis (equations (41) to (43)).The rotation field was probed along a line from $[500, 0.1, -20]$ to $[500, 0.1, 20]$, marked as "line 2" in figure 1 **a)**. Figure 1 **c)** shows the variation of ω_x, ω_y and ω_z along this line. Plotted alongside are $\overline{\omega_y}_S$ and $\overline{\omega_z}_S$, the rotations about the y and z axis for an infinite screw dislocation running along the x axis respectively. ω_z and $\overline{\omega_z}_S$ show good very good agreement. Likewise ω_y and $\overline{\omega_y}_S$ agree very closely. The rise at the center of the ω_y and $\overline{\omega_y}_S$ profiles occurs as "line2" passes not right through the core of the dislocation at $y = 0$, but rather runs at $y = 0.1$. The ω_x rotation is zero, which is consistent with the solution for an infinite screw dislocation along the x axis.

Figures 1 **d),e)** and **f)** show maps of ω_x, ω_y and ω_z rotation respectively, computed for the dislocation triangle ABC on an xz plane intersecting the y-axis at 0.1. The map of ω_x rotation, figure 1 **d)**, shows that no rotation about this axis is present in the edge dislocation segment AB or in the screw dislocation segment BC. This is as expected from the infinite edge and screw dislocation solutions,

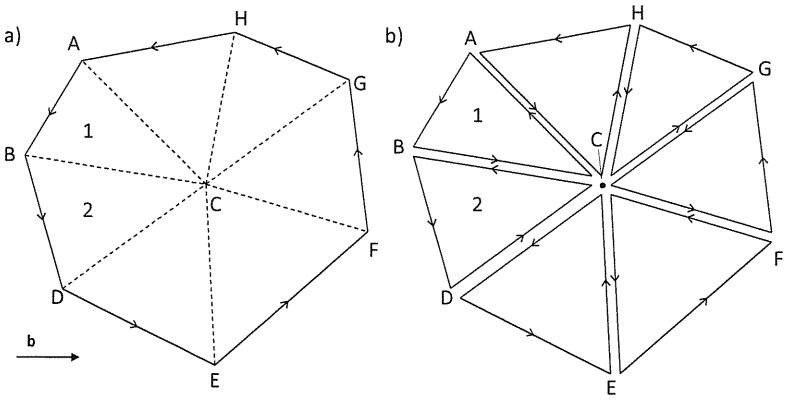

Figure 2. Schematic of a dislocation loop. a) The loop is discretized into dislocation segments. b) for the computation of rotation each dislocation segment is linked to a virtual point C by two virtual segments to give a triangular dislocation loop.

equations (35) to (37) and (41) to (43) respectively. It is interesting to note that the mixed dislocation segment on the other hand has some ω_x rotation component. Also a local maximum of ω_x rotation is present at point B.

The map of ω_y rotation (figure 1 **e)**) shows (as expected from the infinite, two-dimensional edge dislocation solution) that no ω_y rotation is present in the AB pure edge dislocation segment. In the pure screw dislocation segment BC, ω_y some positive rotation is present close to the dislocation core. This is in good agreement with the line plot in figure 1 **c)** and is a result of the mapping plane crossing the y-axis at $y = 0.1$, whilst the plane of the dislocation loop ABC crosses the y-axis at $y = 0$. In the mixed dislocation segment CA it is interesting to note that no ω_y rotation is present.

For this particular dislocation triangle the greatest lattice rotations occur in the ω_z rotation direction (figure 1 **f)**). As would be expected from the expressions for $\overline{\omega_z}_\perp$ and $\overline{\omega_z}_S$, equations (37) and (43) respectively, the rotation field about the edge segment AB is a factor of two greater that the ω_z rotation field of the screw segment BC. It is reassuring to note that the rotation field remains well confined to the dislocation triangle and there do not appear to be any spurious rotations present. Interestingly the area inside the dislocation triangle experiences exclusively positive ω_z rotation, whilst the area outside the triangle experiences exclusively negative ω_z rotation. This observation is consistent with the expected behaviour of the individual dislocation segments when each is considered separately and compared with the two dimensional solution for an infinite dislocation.

4. Lattice rotations arising from a Frank-Read Source

With correct functioning of the basic building block confirmed and the rotation field for a dislocation triangle verified, the rotation fields for more complicated dislocation structures arising in $3D$ can be evaluated. Since the material we have assumed is linearly elastic, superposition can be used to evaluate the total rotation field ω_ξ arising from n dislocation triangles, each giving rise to lattice rotations $\omega_{n\xi}$, where ξ denotes either x, y or z.

$$\omega_\xi = \sum \omega_{n\xi}. \tag{44}$$

Figure 2 **a)** shows a dislocation loop, discretized into segments and with vertices

A, B, D, E, F, G and H. Each dislocation segment has a line direction, indicated by the arrows in figure 2 **a)**, and a Burgers vector, common to all the segments in the loop due to conservation of Burgers vector. To evaluate the lattice rotations ω_x, ω_y and ω_z for this dislocation loop, one possible strategy is to introduce a virtual node C. Linking each vertex of the loop to this point allows the generation of a triangular dislocation loop for each segment. See for example dislocation segment AB in figure 2 **a)**, which is shown as dislocation triangle ABC in figure 2 **b)**. Summing up the rotation fields from the dislocation triangles arising from each segment and node C provides the total lattice rotation field for the dislocation loop. The contributions from the virtual dislocation lines linking the loop vertices to C cancel out. This can be seen clearly in figure 2 **b)**, considering triangles ABC and BDC. Dislocation line BC in triangle ABC and dislocation line CB in triangle BDC have opposite line directions. Since both have the same Burgers vector, their net rotations cancel out. This highlights the importance of closed contours in dislocation loops. Physically a dislocation cannot end inside the lattice. It must rather terminate at a boundary of the lattice, which might be a free surface, a grain boundary or some other obstacle which terminates the lattice. Computationally, a non-closed dislocation loop would lead to the virtual dislocation segments from the ends of the loop not canceling out, thus introducing an artificial closure of the loop. Obviously this is not admissible and hence any dislocation loop should always be closed.

As an example of dislocation-induced $3D$ lattice rotations, the rotation field arising from a Frank-Read Source was considered. The computations to determine the spatial distribution of dislocation segments were carried out using the ParaDiS discrete dislocation dynamics code [34]. An FCC crystal was simulated, which is loaded under uniaxial tension along the 001 crystal axis. A short dislocation segment with $1\bar{1}0$ line direction and Burgers vector $01\bar{1}$ was introduced on the 111 slip plane. Snapshots were taken of the simulation just as the dislocation line is starting to bow out (figures 3 **a)**, **d)** and **g)**), as the dislocation loop curves around the two fixed points (figures 3 **b)**, **e)** and **h)** and as a complete dislocation loop has been formed and the process is about to repeat itself for the emission of the next dislocation loop (figures 3 **c)**, **f)** and **i)**). These three stages will be referred to as I, II and III respectively.

An obvious difficulty is that in the conventional picture of a Frank-Read Source, the source segment does not form a closed loop. It is rather assumed that the ends of the dislocation segment are somehow pinned (e.g. by an obstacle), preventing them from moving. In our simulations, a dislocation segment running in the $\bar{1}\bar{1}\bar{1}$ direction was attached to each end of the Frank-Read Source segment. At a large distance from the simulation plane, a linking segment was introduced. This closes the dislocation loop, whilst, by virtue of being far away from the simulation volume, not disturbing the pattern of lattice rotations produced by the Frank-Read Source.

Lattice rotations were considered in a plane parallel to the 111 crystal plane, which, for figures 3 **a)** - **i)** was aligned such that the x-axis was along the $1\bar{1}0$ direction and the y-axis along the $11\bar{2}$ direction. Furthermore, the plane on which rotations were considered was offset by 0.5 units along the $\bar{1}\bar{1}\bar{1}$ direction from the plane of the Frank-Read Source in order to avoid problems of singularity of solution which arise in the plane of the dislocation loop.

Figures 3 **a)**, **b)** and **c)** show a maps of lattice rotation (in degrees) in the ω_x direction, i.e. about the $1\bar{1}0$ lattice axis. A number of interesting features can be noticed. No artifacts are evident from the virtual dislocations segments which were introduced for the computations of "dislocation triangle" rotation fields. Lattice rotation outside the loop is positive, whilst inside the loop it is consistently negative. At the fixed ends of the Frank-Read Source loop, where the dislocation line runs

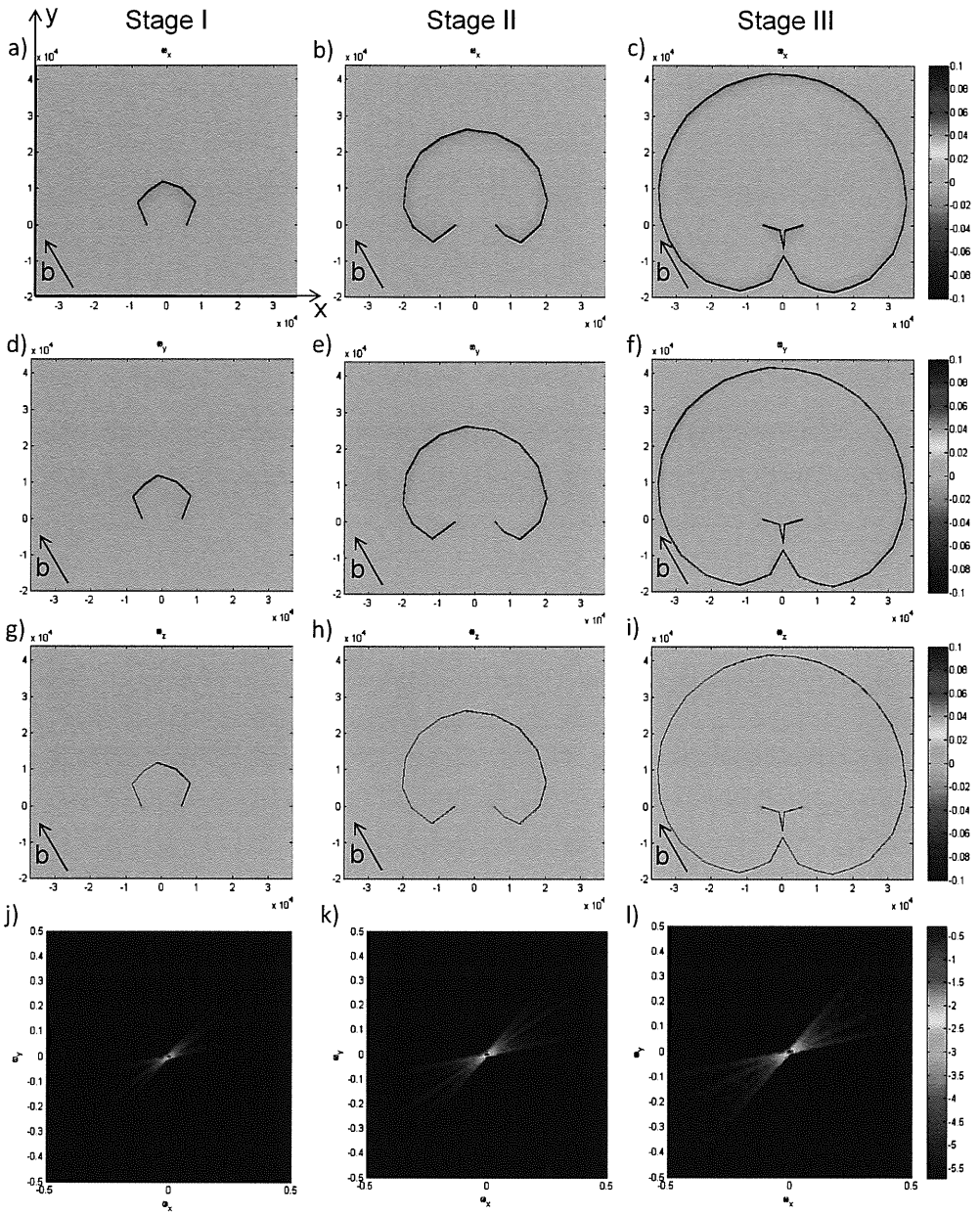

Figure 3. Plots of lattice rotation computed in the plane of a Frank-Read Source on a 111 plane, with Burgers vector $01\bar{1}$. In the plots, the x-axis direction lies along the $1\bar{1}0$ direction and the y-axis corresponds to the $11\bar{2}$ crystal direction. The 111 axis is normal to the plane, coming out of the page. *a*), *b*) and *c*) show plots of ω_x rotations, corresponding to the rotation about the $1\bar{1}0$ direction, for three stages of the Frank-Read loop formation. *d*), *e*) and *f*) show the corresponding ω_y rotations, which are the rotations about the $11\bar{2}$ crystal direction. *g*), *h*) and *i*) are maps of ω_z rotation, about the 111 crystal axis. In all cases the plotting plane was located 0.5 units below the plane of the Frank-Read Source. *j*), *k*) and *l*) show maps of misorientation in the ω_x and ω_y direction for the three stages of evolution of the Frank-Read loop.

perpendicular to the plotting plane, the rotation field decays as expected. In figure 3 **c)**, with one dislocation loop complete, it can be seen that a similar rotation field is established for the next dislocation loop, with positive lattice rotation outside and negative inside the loop. This is as expected from the Burgers vector and line direction configuration. Figures 3 **d)**, **e)** and **f)** show maps of lattice rotation in the ω_y direction, i.e. about the $11\bar{2}$ crystal direction. In this direction lattice rotation is also positive outside the dislocation loop and negative inside. Figures 3 **g)**, **h)**

and **i)** show maps of lattice rotation in the ω_z direction, i.e. about the crystal 111 direction. As expected, since we are close to the plane of the dislocation loop, only little rotation is present in this direction. Interestingly, when zooming into the fixed ends of the Frank-Read Source segment, which are linked to the long dislocation segments in the $\bar{1}\bar{1}\bar{1}$ direction to provide loop closure, the typical edge dislocation rotation field can be seen. The positioning of the positive and negative rotation lobes is as expected from the Burgers vector and dislocation line directions. These edge dislocation fields are consistent in figures 3 **g)**, **h)** and **i)** and their presence confirms the correct functioning of the implementation.

In X-ray diffraction measurements it is difficult to resolve the exact spatial distribution of lattice rotations, due to the limited probe sizes available. Spot sizes of 300nm have become routinely achievable [42] and it is anticipated that smaller beamsizes (sub-100nm) will be available on a day-to- day basis in future. Due to these limitations, it is not possible at present to measure the exact spatial distribution of lattice orientation; rather only the spread of lattice orientations present within the probed gauge volume can be assessed. From particular distributions of lattice orientation within the gauge volume, some conclusions can be drawn about the local dislocation structure present [6] and the active slip systems deduced [15].

It is instructive to look at the spread of lattice orientations introduced by the Frank-Read Source under consideration. Figures 3 **j)**, **k)** and **l)** show $2D$ histograms of ω_x and ω_y orientation for the different stages of the Frank-Read Source formation respectively. Each bin in the histogram has a width of 0.01° in both orientation directions. To highlight the contributions from areas of larger lattice rotation, the number of counts per bin was normalized against the bin with the largest number of counts and then plotted on a log scale. This misorientation map corresponds essentially to the orientation spread which would be seen when projecting a 111 reflection reciprocal space map for this system onto the tangential reciprocal space directions.

In the misorientation maps a number of interesting features can be seen. The orientation spread shows distinct streaking, i.e. elongation in the $+\omega_x/+\omega_y$ to $-\omega_x/-\omega_y$ direction. In fact, the streak consists of a number of individual sub-streaks. The number of sub-streaks increases with the number of dislocation segments as one moves from stage I of the Frank-Read loop to stage II. This suggests that the sub-streaks are in fact an artifact of the discretization of the dislocation loop into discrete segments. If infinitesimal dislocation segments were used for the representation of the Frank-Read loop, the sub-streaks should merge into one. It can also be noted that the streaking direction is consistent between figures 3 **j)**, **k)** and **l)**. If the Frank-Read loop were replaced by straight infinite edge dislocations, with line direction along the $2\bar{1}\bar{1}$ direction, and the same Burgers vector as the Frank-Read Loop, they would give rise to lattice rotation about the $2\bar{1}\bar{1}$ axis. The resulting streaking would be in the same direction in the ω_x, ω_y rotation space as seen here for the Frank-Read Source. This result supports the validity of the methodology used in the literature to determine the active slip system from streaking by considering lattice rotations from a population of infinite, straight edge dislocations on a slip plane [15]. Finally, it can be noted that, as the Frank-Read loop formation progresses, the spread of lattice orientations in the considered volume increases, which is as expected due to increase in dislocation density.

5. Conclusions and Outlook

In this paper a method of evaluating the lattice rotations arising from a distribution of $3D$ dislocation segments within an isotropic elastic medium has been presented.

Based on the solution for the displacement field from a triangular dislocation loop [39–41], expressions for the lattice rotations induced by a triangular dislocation loop have been derived. The predicted rotation field for a simple triangular dislocation loop was compared with $2D$ plane strain solutions for infinite, straight edge and screw dislocations, showing excellent agreement.

Next, the solution was applied to compute the rotation field arising at different stages during the emission of a dislocation loop from a Frank-Read Source. The evolution of the dislocation loop shape was simulated and the dislocation segment positions computed using the ParaDiS discrete dislocation dynamics code [34]. The lattice rotation field showed the expected structure. To study the overall misorientation introduced into the sampling volume by the Frank-Read Source, $2D$ histograms were plotted of lattice orientation. These show distinct streaking patterns related to the Burgers vector orientation for the dislocation loop under consideration. Furthermore, it could be seen that the streaking increases as the evolution of the Frank-Read Source progresses, a phenomenon well-known from experimental investigations.

The solution presented here makes it possible to compute the lattice rotation fields arising from any arbitrary $3D$ dislocation arrangements which could be computed by discrete dislocation dynamics simulation. The rotation fields can be used to compute predicted diffraction patterns for direct comparison with experimental diffraction measurements [18]. This would be particularly useful for the investigation of phenomena such as dislocation substructure formation, where, due to the limits on the experimental spatial resolution, comparison with simulations should play an essential role in ensuring correct interpretation and understanding of the fundamental deformation mechanisms at work. Furthermore, the lattice rotations could be used to inform discrete dislocation dynamics codes of the local reorientation of slip planes, an effect which thus far in $3D$ simulations has been assumed to be small, but was shown to be of importance in two dimensions [43–45].

References

[1] D.A. Hughes, Scripta Materialia 47 (2002) p.697–703.
[2] X. Huang, Scripta Materialia 38 (1998) p.1697–1703.
[3] U. Essmann, M. Rapp and M. Wilkens, Acta Metallurgica 16 (1968) p.1275–1287.
[4] D. Breuer, P. Klimanek and W. Pantleon, Journal of Applied Crystallography 33 (2000) p.1284–1294.
[5] P. Cizek, Scripta Materialia 45 (2001) p.815–822.
[6] B. Jakobsen, H.F. Poulsen, U. Lienert, J. Almer, S.D. Shastri, H.O. Sorensen, C. Gundlach and W. Pantleon, Science 312 (2006) p.889–892.
[7] P.F. Fewster, Critical Reviews in Solid State and Materials Sciences 22 (1997) p.69 – 110.
[8] B. Jakobsen, H.F. Poulsen, U. Lienert and W. Pantleon, Acta Materialia 55 (2007) p.3421–3430.
[9] B. Jakobsen, U. Lienert, J. Almer, H.F. Poulsen and W. Pantleon, Materials Science and Engineering: A 483-484 (2008) p.641–643.
[10] B. Jakobsen, H.F. Poulsen, U. Lienert, J. Bernier, C. Gundlach and W. Pantleon, physica status solidi (a) 206 (2008) p.21–30.
[11] J.D. Budai, W. Yang, N. Tamura, J.S. Chung, J.Z. Tischler, B.C. Larson, G.E. Ice, C. Park and D.P. Norton, Nat Mater 2 (2003) p.487–492.
[12] H. Yan and I.C. Noyan, Journal of Applied Physics 98 (2005) p.073527–6.
[13] F. Hofmann, B. Abbey, X. Song, I. Dolbnya and A.M. Korsunsky, International Journal of Modern Physics B 24 (2009) p.279287.
[14] F. Hofmann, X. Song, I. Dolbnya, B. Abbey and A.M. Korsunsky, Procedia Engineering 1 (2009) p.193–196.
[15] R. Barabash, G.E. Ice, B.C. Larson, G.M. Pharr, K.S. Chung and W. Yang, Applied Physics Letters 79 (2001) p.749–751.
[16] R.I. Barabash, G.E. Ice and F.J. Walker, Journal of Applied Physics 93 (2003) p.1457–1464.
[17] G.E. Ice, R.I. Barabash and F.J. Walker, Composites Part B: Engineering 36 (2005) p.271–277.
[18] F. Hofmann, X. Song, S. Eve, S.P. Collins and A.M. Korsunsky, Materials Letters 63 (2009) p.1077–1081.
[19] X. Song, *Modelling Residual Stresses and Deformation in Metal at Different Scales*, Universitsy of Oxford, 2010.
[20] E. GiessenVan der and A. Needleman, Modelling and Simulation in Materials Science and Engineering 3 (1995) p.689–735.

[21] L. Nicola, E. GiessenVan der and A. Needleman, Journal of Applied Physics 93 (2003) p.5920–5928.
[22] L. Nicola, Y. Xiang, J.J. Vlassak, E. GiessenVan der and A. Needleman, Journal of the Mechanics and Physics of Solids 54 (2006) p.2089–2110.
[23] E. Bittencourt, A. Needleman, M.E. Gurtin and E. GiessenVan der , Journal of the Mechanics and Physics of Solids 51 (2003) p.281–310.
[24] A. Widjaja, A. Needleman and E. GiessenVan der , Modelling and Simulation in Materials Science and Engineering 15 (2007) p.121–132.
[25] A. Widjaja, E. GiessenVan der and A. Needleman, Acta Materialia 55 (2007) p.6408–6415.
[26] D.S. Balint, V.S. Deshpande, A. Needleman and E. GiessenVan der , Journal of the Mechanics and Physics of Solids 54 (2006) p.2281–2303.
[27] A. Widjaja, E. GiessenVan der and A. Needleman, Materials Science and Engineering A 400-401 (2005) p.456–459.
[28] V.S. Deshpande, A. Needleman and E. GiessenVan der , Acta Materialia 51 (2003) p.1–15.
[29] V.S. Deshpande, A. Needleman and E. GiessenVan der , Acta Materialia 51 (2003) p.4637–4651.
[30] D.S. Balint, V.S. Deshpande, A. Needleman and E. GiessenVan der , Materials Science and Engineering A 400-401 (2005) p.186–190.
[31] D.S. Balint, V.S. Deshpande, A. Needleman and E. GiessenVan der , Modelling and Simulation in Materials Science and Engineering 14 (2006) p.409 – 422.
[32] G. Gaucherin, F. Hofmann, J.P. Belnoue and A.M. Korsunsky, Procedia Engineering 1 (2009) p.241–244.
[33] A.A. Benzerga, Y. Brechet, A. Needleman and E. GiessenVan der , Modelling and Simulation in Materials Science and Engineering 12 (2004) p.159–196.
[34] V.V. Bulatov and W. Cai *Computer Simulations of Dislocations*, Oxford University Press, 2006.
[35] A. Arsenlis, W. Cai, M. Tang, M. Rhee, T. Oppelstrup, G. Hommes, T.G. Pierce and V.V. Bulatov, Modelling and Simulation in Materials Science and Engineering 15 (2007) p.553–596.
[36] V.V. Bulatov, W. Cai, J. Fier, M. Hiratani, G. Hommes, T.G. Pierce, M. Tang, M. Rhee, K. Yates and T. Arsenlis, *Scalable line dynamics in ParaDiS*, in *Conference on High Performance Networking and Computing*, 2004.
[37] W. Cai and V.V. Bulatov, Materials Science and Engineering A 387-389 (2004) p.277–281.
[38] V.V. Bulatov, L.L. Hsiung, M. Tang, A. Arsenlis, M.C. Bartelt, W. Cai, J.N. Florando, M. Hiratani, M. Rhee and G. Hommes, Nature 440 (2006) p.1174–1178.
[39] D.M. Barnett, Philosophical Magazine A 51 (1985) p.383 – 387.
[40] D.M. Barnett and R.W. Balluffi, Philosophical Magazine Letters 87 (2007) p.943 – 944.
[41] , ????
[42] G.E. Ice, J.W.L. Pang, B.C. Larson, J.D. Budai, J.Z. Tischler, J.Y. Choi, W. Liu, C. Liu, L. Assoufid, D. Shu and A. Khounsary, Materials Science and Engineering: A 524 (2009) p.3–9.
[43] V.S. Deshpande, A. Needleman and E. GiessenVan der , Journal of the Mechanics and Physics of Solids 51 (2003) p.2057–2083.
[44] V.S. Deshpande, A. Needleman and E. GiessenVan der , Materials Science and Engineering A 400-401 (2005) p.154–157.
[45] V.S. Deshpande, A. Needleman and E. GiessenVan der , Journal of the Mechanics and Physics of Solids 53 (2005) p.2661–2691.